Characterization of lift force and torque in prolate ellipsoid suspensions

Ze Cao[1], Danesh K. Tafti[2,*]

[1] *School of Hydraulic Engineering, Dalian University of Technology, Dalian 116024, China*

[2] *Department of Mechanical Engineering, Virginia Tech, Blacksburg, VA 24061, USA*

Abstract

The paper derives correlations for lift force and fluid torques acting on stationary prolate ellipsoid suspensions of aspect ratio (AR) 2.5, 5, and 10 subjected to uniform flow. Particle Resolved Simulations (PRS) are conducted on a suspension of infinite extent in two directions for Reynolds number $10 \leq Re \leq 200$ and solid fractions (φ) between $0.1 \leq \varphi \leq 0.3$. The suspension-mean lift-to-drag ratio varies between 7% to 14% at Re=10 which increases to 14%~22% at Re=200. The torque-induced tip rotational acceleration can reach 38% ~ 85% of drag-induced translational acceleration at $Re = 200$. Single particle lift force and torque correlations of [1] are modified and adapted to predict current angular-mean lift and torque data. The resulting lift correlation captures the PRS data within an average deviation below 7%. Torque exhibits a somewhat more complex dependency at AR=10 than the assumed $sin\theta \cdot cos\theta$ variation but nevertheless the correlations predict angular-mean values with mean relative deviations of 16.6% at AR=10.

Keywords: Lift force, Torque, Ellipsoidal particle suspension; Correlations; Particle Resolved Simulations; Immersed Boundary Method (IBM)

1. Introduction

In fluid-particle systems, modeling the drag force has received much attention in the literature for both spherical [2–5] and non-spherical [6–11] particles. However, unlike spherical particles, asymmetric geometries and orientations of non-spherical particles lead to flow asymmetries in

* Corresponding author: 213E Goodwin Hall, 635 Prices Fork Rd., Blacksburg, VA 24061. Ph. (540)231-9975: email: dtafti@exchange.vt.edu

directions other than the flow direction resulting in lateral forces that are perpendicular to drag. Taking rotational symmetric geometries like ellipsoids [12] and cylinders [13] as examples, a lift force is defined in the plane composed of the particle's rotational symmetry axis and the vector along the flow direction with direction perpendicular to the flow direction. Similar to the effect of drag, lift induces lateral motions with respect to flow direction. This can have a large impact on particle trajectory and thereby influence the solid phase mixing rate. To stress the significance of lift, Vakil & Green [13] performed Particle Resolved Simulation (PRS) for an isolated cylinder in the flow. They studied aspect ratios (abbreviated as AR, defined as ratio between height L and diameter D of the cylinder) of 2 to 20 for Reynolds number ($Re_D = \frac{\rho U_\infty D}{\nu}$) between 1 and 40. The calculated ratio between lift and drag (F_L/F_D) reached a maximum value of 0.16 to 0.40 at inclination angles between 30° and 40° as the cylinder aspect ratio increased from 2 to 20 at $Re_D = 40$, showing the non-negligible magnitude of lift forces on non-spherical particle. Furthermore, the significance of lift in complex fluid-particle systems has also been demonstrated by He & Tafti [14]. Their PRS simulations for AR2.5 ellipsoid suspensions at solid fraction (φ) from 0.1 to 0.35 found that the portion of particles having F_L/F_D larger than 0.1 was 20% at $Re = 10$, which increased to approximately 80% and 60% at $Re = 200$ for solid fractions of 0.1 and 0.35, respectively. Similarly, Sanjeevi & Padding [15] simulated flow through AR4 sphero-cylinder suspensions. In their observation, the percentage of particles with $\frac{F_L}{F_D} > 0.1$ was 80% at $Re = 100$ with over 30% of the particles possessing F_L/F_D > 0.3. These observations signify the increasing contribution of lift forces with Re and particle aspect ratio for prolate particle geometries. The effect of particle inclination angle (θ) on F_L/F_D was also investigated by Cao & Tafti [16] by performing PRS for AR0.25 cylinder suspensions at solid fraction of 0.1, 0.2 and 0.3. In spite of the very different geometry and flow conditions, the inclination angle at which $|F_L|/F_D$ of the AR0.25 cylinders reached a peak value was similar to that for isolated cylinders [13] near $\theta = 30°$ with magnitude of 0.2 at $Re = 10$, increasing to 0.5 as Re increased to 300.

Correlations proposed in the literature for isolated cylinders [13,17] and ellipsoids [12,18,19] can be generalized (with some modifications) as $F_L = A \cdot sin(\theta)\cos(\theta)$ with A being a function of Re and particle geometry to capture the peak lift defined to occur at $\theta = 45°$. This form was also found to be applicable to suspensions of AR4 sphero-cylinder suspensions [15] at Reynolds

number between (0.1, 1000) and solid fraction between (0.1, 0.5). However, broader applicability of this form is limited by the narrow range of particle geometries [12,17,19] and Reynolds numbers [13] considered. Thus, poor prediction accuracy [18] has been observed in other work [1,19]. Fröhlich et al. [1] simulated flow over isolated ellipsoids of aspect ratios ranging from 2 to 8 for $Re \in [1, 100]$. They validated both drag and lift with [20] and [19], respectively, to emphasize the strong reliability of their correlation in calculating momentum exchange between the fluid and solid phase.

In addition to lift, the non-uniform distribution of flow velocity and pressure around an inclined non-spherical particle will also result in pitching torque and cause rotational motion of the particles. Most of the above-mentioned studies [1,12,13,17,19,21] have also proposed correlations for pitching torque. Cao & Tafti [16] demonstrated the significance of flow induced torque by comparing with the collision induced torque. For biomass particles, fluid induced torque was comparable to collision induced torque and concluded to have a dominant effect on particle transport.

Compared to drag forces, the inclusion of fluid lift and torque to fluid-particle dynamics in suspensions has largely been ignored because of the predominant emphasis and use of the spherical particle assumption in the literature. However, in the past decade the capability to simulate non-spherical particles has increased substantially and the inclusion of all relevant forces and torques in simulating particle dynamics has become more urgent in order to exploit the full fidelity of non-spherical particle simulations. The objective of this paper is to develop correlations for lift and torque for stationary ellipsoidal particle suspensions using Particle Resolved Simulations (PRS). Ellipsoids of aspect ratio 2.5, 5 and 10 are simulated in the Re range of (10, 200) and solid fractions of 0.1, 0.2 and 0.3. These ranges of conditions are relevant to bubbling fluidized beds in which steady fluid forces play a dominant role in system dynamics [22,23]. It is shown that both lift and torque contribute substantially to particle motion and mixing. Section 2 outlines the computational setup employed and validation of the numerical procedure and grid resolution used for the simulations. Section 3 presents the lift and torque results and their relative significance with respect to drag force on particle transport. Correlations for calculating mean lift and torque over the range of conditions are developed. Finally, the main conclusions are listed in section 4.

2. Methodology

2.1. Governing Equations

The dimensionless constant property mass and momentum conservation equations governing fluid flow in the particle suspension are expressed as:

Continuity:

$$\frac{\partial u_i}{\partial x_i} = 0 \tag{1}$$

Momentum:

$$\frac{\partial u_i}{\partial t} + \frac{\partial}{\partial x_j}\left(u_i u_j\right) = -\frac{1}{\rho}\frac{\partial p}{\partial x_i} + \frac{\partial}{\partial x_j}\left\{\frac{1}{Re}\left(\frac{\partial u_i}{\partial x_j}\right)\right\} \tag{2}$$

with the following non-dimensionalizations

$$u_i = \frac{u_i^*}{u_{ref}^*};\ x_i = \frac{x_i^*}{l_{ref}^*};\ \ p = \frac{p^* - p_{ref}^*}{\rho_{ref}^* u_{ref}^{*\,2}};$$

$$\rho = \frac{\rho^*}{\rho_{ref}^*};\ \mu = \frac{\mu^*}{\mu_{ref}^*};\ \ Re = \frac{\rho_{ref}^* u_{ref}^* l_{ref}^*}{\mu_{ref}^*}$$

Superscript (*) is used to denote dimensional variables whereas the absence of superscripts denote dimensionless variables. The undisturbed free stream velocity U_∞^* is taken as u_{ref}^* and l_{ref}^* is defined as the particle's volume equivalent sphere diameter d_{eq}^*. An in-house CFD code – GenIDLEST (Generalized Incompressible Direct and Large Eddy Simulation of Turbulence) is employed to solve the governing equations with the Immersed Boundary Method (IBM) for resolving the particles in the suspension.

Based on a non-staggered grid topology, the governing equations are solved using the finite-volume procedure combined with the second order central differencing scheme [24,25]. With the fluid domain decomposed into multi-block structured orthogonal grids, the flow variables including velocity and pressure are calculated and stored at the cell centers whereas mass fluxes are stored at the cell surfaces. The advancement in time is achieved by a predictor-corrector method: an intermediate velocity field is firstly calculated in the predictor step, followed by the

corrector step that corrects the flow velocity, based on the solution of a pressure equation, to satisfy discrete continuity.

2.2. Particle Details and Immersed Boundary Method

The ellipsoids investigated in this study are generated using the implicit surface formulation in Cartesian coordinate system that can be written as:

$$\left(\frac{x}{l_a}\right)^2 + \left(\frac{y}{l_b}\right)^2 + \left(\frac{z}{l_c}\right)^2 = 1 \tag{3}$$

with l_a, l_b and l_c defining the semi-axis length of the ellipsoid along its three principal axis. In this study, ellipsoids with aspect ratio of 2.5, 5 and 10 are investigated and the detailed geometrical information about these particles can be found in our previous study [26]. To calculate the force and torque vectors for each particle, a local coordinate system is established for each particle in the suspension exemplified in Fig. 1 for a AR5 particle. The local coordinate system originates from the particle geometrical center with the x'-axis coinciding with the undisturbed flow direction. By defining a vector $\vec{l} = (x_l, y_l, z_l)$ from the local coordinate system origin to one of the ellipsoid poles having larger *x*-coordinate value as is plotted in Fig. 1, a unit vector along the y'-axis is derived using $\vec{n}_y = (0, y_l, z_l)/sqrt(y_l^2 + z_l^2)$, followed by the z'-axis which is determined based on the right-hand rule. The particle inclination angle is defined as the angle between x'-axis and rotational symmetry axis of the particle with a range between 0° to 90°. Drag force F_D is defined as the $x' -$ direction component of the total fluid-particle interaction force [27,28], with the $y' -$ directional forces defined as the lift force F_L, and the $z' -$ direction force as the lateral force which has a zero mean. While not the subject of this paper, lateral forces on individual particles can have substantial deviations from the zero mean value.

On the basis of calculated hydrodynamic force acting on each triangular surface element, the torque vector about the center of mass of the particle is derived using:

$$\vec{T} = \sum_{surface} \vec{r}_e \times \vec{F}_e \tag{4}$$

where $\vec{F}_e$ is the total hydrodynamic force on the surface element and $\vec{r}_e$ denotes the vector from particle center of mass to the surface element centroid. Following the orthogonal decomposition

of torque in the local coordinate system, mean torques about both x'- and y'-axis are observed to have near-zero magnitudes due to the symmetry of the ellipsoid with respect to the $x' - y'$ plane. Therefore, primarily pitching torque, $T_{z'}$ is investigated – it has by far the largest sustained effect on particle motion.

Fig. 1. Local Cartesian coordinate system with the definition of lift and torque for AR5 ellipsoid

The applied immersed boundary method in our simulation was initially developed and validated by Nagendra et al. [29]. In the application of IBM, structured orthogonal background grids are generated for resolving the fluid, within which the particle surface represented by a surface mesh composed of triangular elements, is immersed as presented in Fig. 1. The number of surface elements adopted for each AR2.5, AR5 and AR10 ellipsoids are 2172, 4176 and 7538, respectively. Three different types of background grid nodes are defined, those that reside completely inside or outside of the immersed surface are classified as fluid and solid nodes, respectively. The remaining background nodes that lie adjacent to the immersed surface with centroids located outside are defined as fluid IB nodes. Probes are defined for these fluid IB nodes along the outward normal direction of the immersed surface with the primitive flow variables interpolated from surrounding fluid nodes to the probe locations. Combined with the no-slip, no-penetration boundary conditions at the particle surface, primitive flow variables of the fluid IB nodes are derived using Taylor series expansion. In solving the mass and momentum equations for the fluid nodes, the fluid IB nodes serve as the *de facto* location of boundary conditions to signal the presence of the particle surface [29]. During post-processing, another series of probes are assigned for each surface element along its normal direction that extend into the fluid. The interpolated flow velocity and pressure at the probe locations are used to derive the viscous and pressure forces acting on the particle surface [17].

2.3. Computational Domain

The current simulation setup is the same as that used in Cao et al. [27]. As presented in Fig. 2, a rectangular computational domain with dimensions of $30 \times 10 \times 10$ along $x -$ $y -$ and $z -$ directions, respectively is used. The particles are distributed in the region $5 \leq x \leq 20$. A uniform fluid velocity with non-dimensional magnitude of unity is specified at the inlet. The

outlet is assigned a zero gradient condition for both pressure and velocity. Periodic boundary conditions are used in the $y-$ and $z-$ directions to simulate an infinitely large suspension along these directions.

Fig. 2. Computational domain for the PRS simulations.

The random particle suspensions are generated using PhysX [30] from Nvidia and the procedure is outlined in Cao et al. [27]. Particles are continuously added in the domain at random locations with non-zero velocities. The physics engine PhysX detects overlaps and resolves collision between particles till the desired solid volume fraction is reached. The number of particles range from 286 to 859 for solid fractions of 0.1 to 0.3. For each solid fraction investigated, two independent suspensions are used for AR5 and AR10 ellipsoids whereas one arrangement generated in this study combined with 3 other arrangements investigated by He & Tafti [14] are used for the AR2.5 ellipsoids. A $z-$plane of the computational domain showing the $x-$directional velocity of the flow generated by a AR10 ellipsoid suspension of $\varphi = 0.1$ at Re=10 and 200 is plotted in Fig. 3. Both $Re = 10$ and 200 exhibit a smooth flow transmission at the outflow boundary in spite of the u-velocity not being uniform at the exit plane opening up the possibility that the outflow boundary condition could impact the flow in the suspension by the upstream propagation of disturbances introduced at the exit. However, the weak disturbance propagating from the domain exit boundary would be overwhelmed by the flow disturbance caused by the particles at the suspension exit. As a consequence, it is very unlikely that the flow inside the suspension beyond the last 1 or 2 rows of particles is affected by the existence of the domain outflow boundary 20 diameters downstream from the exit to the suspension.

Fig. 3. u-velocity distribution in AR10 ellipsoid suspension at φ=0.1

2.4. Grid Independency and Validation

Extensive grid independency investigations on the IBM have been conducted over the course of many past studies on characterizing fluid forces in ellipsoidal suspensions [31] [27] [17]. Since particles in suspension exist as individual particles, grid independency is typically done for

isolated particles in a flow, and then followed up with a few studies in representative suspensions. Various particle shapes have been considered starting from spherical shapes to ellipsoids (AR2.5 and 10) used in this study to low aspect ratio cylinders (AR0.25).

He at al. [31] evaluated grid resolutions of $\frac{1}{30}d_{eq}$, $\frac{1}{40}d_{eq}$ and $\frac{1}{50}d_{eq}$ in PRS of AR2.5 ellipsoidal suspension in the range $10 \leq Re \leq 200$. They showed that the maximum difference between the $\frac{1}{30}d_{eq}$ and $\frac{1}{50}d_{eq}$ grid was about 2.2% which decreased to 1.6% for $\frac{1}{40}d_{eq}$ grid spacing and used the $\frac{1}{40}d_{eq}$ grid for their calculations. This was followed by a grid independency study in AR10 suspension at $\varphi = 0.2$ and $Re = 200$ by Cao et al. [27] in which they compared background grid resolutions of of $\frac{1}{40}d_{eq}$ and $\frac{1}{50}d_{eq}$. They found that more than 97% of the ellipsoids from the $\frac{1}{40}d_{eq}$ grid showed deviation of drag force of less than 2.5% with respect to the $\frac{1}{50}d_{eq}$ grid, indicating that the background grid spacing of $\frac{1}{40}d_{eq}$ provided very good fidelity for the AR10 shapes also. Similar conclusions were reached by Cao and Tafti [17] for isolated AR0.25 cylindrical particles placed at different inclination angles to the flow at $Re = 10$ and 200. Using the drag force derived from the $\frac{1}{50}d_{eq}$ grid as a reference, the relative deviation of drag force on the $\frac{1}{30}d_{eq}$ grid averaged at 2.16% with a maximum deviation of 4.45% over the range of Re and particle inclination angles investigated. The average and maximum deviations of $\frac{1}{40}d_{eq}$ grid were 0.85% and 1.7%, respectively. In the same study, the predicted drag force of an isolated sphere [17] using IBM was compared to experimental [20,32] and computational [33] results in the literature, and a body-fitted grid using a grid size of $\frac{1}{40}d_{eq}$. A maximum deviation of 4.8% was observed in the range $10 \leq Re \leq 300$ with the body-fitted grid at $Re = 300$. In addition, the PRS simulations for spherical particle suspensions performed by He et al. [31] using a grid size of $\frac{1}{40}d_{eq}$ found good agreement of suspension mean drag force with the numerical results of Tenneti et al. [5] in the range $0.1 \leq \varphi \leq 0.45$ and $10 \leq Re \leq 200$. Based on the numerous validating results obtained over the course of past studies, results from a background grid size of $\frac{1}{40}d_{eq}$ are reported in this paper.

2.5. Data Processing

Similar to drag force, the lift forces are non-dimensionalized by the Stokes drag:

$$F_L = \frac{F_L^*}{3\pi\mu^* U_\infty^* d_{eq}^*} \tag{5}$$

while the torques are non-dimensionalized using:

$$T = \frac{T^*}{\frac{3}{2}\pi\mu^* U_\infty^* d_{eq}^{*2}} \tag{6}$$

In the investigation on drag forces [27], it was observed that the drag force on a particle was dependent on its relative location with respect to the entrance and exit planes of the suspension and only particles which were sufficiently "deep" in the suspension were considered in the drag force analysis. The same is evaluated for lift forces and torques with representative distributions plotted in Fig. 4 for AR10 ellipsoids at $Re = 10$ and $\varphi = 0.2$. The lift forces F_L show no visible trends in the flow direction exhibiting a relatively constant mean value at each $x-$location. On the other hand, the torque $T_{z'}$ exhibits sensitivity to the particle proximity to the suspension entrance and exit planes. After surveying all the results, particles centered between $7 \leq x \leq 18$ were used for further analysis.

Fig. 4. Individual AR10 ellipsoid F_L and $T_{z'}$ with respect to their centroid x-location in suspension with $\varphi = 0.2$, $Re = 10$

3. Results and Discussion

3.1. Lift characteristics

Lift forces on AR10 ellipsoids, $\varphi = 0.2$ suspensions with respect to particle inclination angles are presented in Fig. 5. It is noted that in the right-handed local coordinate system defined by (x', y', z'), the particle lift forces F_L are predominantly negative and thus for presentation purposes, $-F_L$ is plotted. Each green dot represents an individual particle in the suspension while blue dots are averaged lift force $\bar{F}_{L,\theta}$ together with their standard deviation (*SD*) within a θ range of 10°, i.e., $[0°, 10°]$, $[10°, 20°]$ … till $[80°, 90°]$. The median of each interval is selected as the representative inclination angle for plotting $\bar{F}_{L,\theta}$. The large scatter in individual particle lift force for any given range of inclination angles is indicative of the sensitivity of lift force to the local flow conditions induced by surrounding particles. Because of this, it is noted that a particle can

experience positive lift even at $\theta \cong 45°$ when nominally the lift force on an isolated particle reaches a peak negative value [1,18]. While positive and negative lift forces are experienced by individual particles, the mean lift remains negative and symmetric about the peak at $\theta = 45°$ for $Re = 10$, but notably shifts to near $\theta = 55°$ at $Re = 200$. The shift in peak lift to higher angles for high aspect ratio and Reynolds numbers has also been observed in past studies by Vakil & Green [13] for isolated cylinders with aspect ratio between 2 and 20 and by Ouchene et al. [21] for isolated ellipsoids with aspect ratio between 1.25 and 5.

Fig. 5. Individual (F_L) and inclination mean lift forces ($\bar{F}_{L,\theta}$) with standard deviation of AR10 ellipsoid suspension at $\varphi = 0.2$

Further insight into lift force fluctuations is gained by studying the coefficients of variation (*CV*), i.e., ratio of standard deviation relative to the mean lift within different angular intervals. The CV has significance when attempting to model lift force by a representative mean value, and is indicative of the possible deviation of the actual instantaneous lift force from the mean. Results for AR2.5 and AR10 ellipsoids are plotted in Fig. 6. There are two notable trends: the first is that CV increases as $\theta \to 0°$ and 90° and the other is that as Re decreases, CV increases. The first is explained by the observation that at these limits $\overline{F}_{L,\theta} \to 0$ and any finite positive or negative fluctuation will result in large CV. The increasing trend in CV with Re can be explained from our previous work [28] in which it was shown that as Re decreases to $Re = 10$, the viscosity dominated flow has larger magnitudes of positive and negative velocity fluctuations about the mean, which consequently lead to larger fluid force fluctuations about the mean. As Re increases the effect of particles on flow is more localized and has less of an effect on surrounding particles. Besides these two main trends, the CV also has a weak dependence on φ which decreases as AR increases from 2.5 to 10.

Fig. 6. Coefficients of variation (*CV*) with respect to θ for different particle suspensions

The suspension mean lift force $\bar{F}_L$ and mean lift/drag force ratio calculated using:

$$\bar{\xi} = \frac{1}{n}\left(\sum_{i=1}^{n} \frac{F_{L,i}}{F_{D,i}}\right) \quad (7)$$

where n is the total number of particles in the suspension are plotted in Fig. 7(a) and Fig. 7(b), respectively. The normalized mean lift force $\bar{F}_L$ ranges from values less than 1 at AR2.5, $Re = 10$ and $\varphi = 0.1$ to greater than 7 at $Re = 200$ and the force ratio $\bar{\xi}$ increases likewise from values as low of 0.06 at $Re = 10$ to 0.23 at $Re = 200$. On the other hand, while $\bar{F}_L$ increases with φ, the force ratio decreases, indicating that even though both lift and drag forces increase with φ, the drag forces increase more than lift. A somewhat different trend is observed in $\bar{\xi}$ for AR2.5 ellipsoid suspensions at $Re = 10$, for which $\bar{\xi}$ becomes independent of φ, indicating that at these conditions drag and lift reduce proportionally at all solid fractions. Overall, the mean lift force is 6%~14% of the drag force at $Re = 10$ for different ellipsoid suspensions and increases to approximately 13%~22% at $Re = 200$.

Fig. 7. Suspension mean lift force of different ellipsoids. (Red: AR2.5 ellipsoid; Green: AR5 ellipsoid; Blue: AR10 ellipsoid)

Fig. 8 presents the variation of individual particle lift-to-drag ratio (ξ) and angular mean ($\bar{\xi}_\theta$) at $Re = 10$ and 100 for AR2.5 particles at $\varphi = 0.1$. In spite of positive and negative fluctuations of individual particle force ratios, the mean angular force ratio follows the same trend as the lift force, reaching a peak value at near 45°. It is observed that $Re = 10$ is more prone to negative lift forces than $Re = 100$ and hence exhibits smaller mean force ratios. At $Re = 200$, the force ratio presents a much stronger dependence on the particle inclination angle and most of the negative lift disappears. As a result, a higher overall $\bar{\xi}$ is derived. A maximum lift-drag ratio always appears within θ of $[35°, 45°]$ among the ellipsoids with different aspect ratios, showing maximum $\bar{\xi}_\theta$ ~ 0.1 at $Re = 10$, $\varphi = 0.1$ which increases to 0.3 and higher at $Re = 200$ at $\varphi = 0.1$.

Fig. 8. Individual and averaged particle lift/drag ratio in AR2.5 ellipsoid suspension at $\varphi = 0.1$, $Re = 10$ (left) and 200(right).

3.2. Proposed Lift Correlation

Abundant effort has been put on proposing correlations for an isolated ellipsoid [1,12,18,21]. While ellipsoid suspensions follow the same approximate trend with particle inclination as an isolated particle the magnitudes are notably different as Re and φ increase [14]. Considering that most studies [14,15,34] have focused on a specific geometry or aspect ratio to investigate lift force, here we attempt to develop a more general correlation for ellipsoidal suspensions.

Based on the linearity of the Navier-Stokes equations in the Stokes regime, Happel and Brenner [35] derived the lift correlation for an isolated ellipsoid in the flow with the form of:

$$F_{L,cor} = \left(F_{D,\theta=90^\circ} - F_{D,\theta=0^\circ}\right) sin(\theta)\, cos(\theta) \quad (8)$$

where $F_{D,\theta=0^\circ}$ and $F_{D,\theta=90^\circ}$ are the drag forces at $\theta = 0°$ and $90°$. Sanjeevi & Padding [15] used Eq. (8) for AR4 sphero-cylinder suspensions for correlating their PRS obtained lift forces for solid fractions and Reynolds numbers up to of 0.5 and 1000, respectively, and found reasonable agreement. Encouraged by their results, the applicability of Eq (8) is evaluated for correlating the lift forces in the current study. The results for AR2.5 and AR10 suspensions are presented in Fig. 9 While Eq. (8) does a reasonable job for AR2.5 ellipsoid suspensions, agreement with PRS data for AR10 ellipsoid suspensions is limited to $Re = 10$, beyond which the deviation increases with increasing Re. Similar trends are also observed for the AR5 ellipsoid. Therefore, it can be inferred that Eq. (8) derived from an isolated ellipsoid in the flow still holds for particle suspensions within the low aspect ratio, low Reynolds number regime.

Fig. 9. Comparison of F_L derived from PRS simulation and Eq (8) for different ellipsoid suspensions

Towards developing a lift correlation that is applicable from dilute fluid-particle systems to particle suspensions with moderate solid fractions, we start from the lift correlation proposed for an isolated ellipsoid in the flow. Hölzer and Sommerfeld [36] performed Lattice-Boltzmann simulations for an AR1.5 ellipsoid and observed that symmetricity of the lift force distribution with respect to $\theta = 45°$ is broken at $Re \geq 30$. On the other hand, results from Zastawny et al. [12] for an isolated AR2.5 ellipsoid observed poor accuracy of the lift correlation which modeled

the maximum lift force on the basis of drag. Therefore, Zastawny et al. [12] modified Eq (8) to take a more general form:

$$C_{L,iso} = A \cdot \sin(\psi)\cos(\psi) \tag{9}$$

where $C_{L,iso} = \frac{F_L^*}{\frac{1}{2}\rho^* U_\infty^{*2} \cdot \pi d_{eq}^{*2}/4}$ represents the lift coefficient. A is a function of Reynolds number that is twice the maximum lift coefficient while ψ denotes a modified inclination angle to account for the skewness of the lift force towards higher inclination angles for $Re > 1$. Similar formulations have also been implemented by researchers for ellipsoids of different aspect ratios and Reynolds numbers [18,19], demonstrating the latent generalizability of Eq (9) in modeling ellipsoid lift force. This was verified in a recent study carried out by Fröhlich et al. [1]. With A and ψ properly modeled, deviations between the results from their proposed correlation based on Eq. (9) and PRS simulations was shown to be less than 5% for ellipsoids with $2 \leq AR \leq 8$ at $1 \leq Re \leq 100$. In this study, the suspension angular mean lift model is built on the correlation proposed by Fröhlich et al. [1] for resolving the lift force in fluid-particle systems approaching the dilute limit. Their correlation replaces A in Eq (9) by $2C_{L,max}$ where $C_{L,max}$ is the maximum lift that is derived from:

$$C_{L,max} = (1 + 0.34Re^{0.88-0.05\ln(AR)})\frac{C_{D,Stokes,90} - C_{D,Stokes,0}}{2} \tag{10}$$

with $C_{D,Stokes,90}$ and $C_{D,Stokes,0}$ calculated using:

$$C_{D,Stokes,0} = \frac{64AR^{2/3}}{Re}\frac{1}{\frac{\chi_0}{\chi_1^2} + AR^2\chi_2} \tag{11}$$

$$C_{D,Stokes,90} = \frac{64AR^{2/3}}{Re}\frac{1}{\frac{\chi_0}{\chi_1^2} + AR^2\chi_3} \tag{12}$$

In Eq (11-12), $\chi_1 = d_{eq}/(2AR^{1/3})$ while χ_0, χ_2 and χ_3 are shape parameters defined as:

$$\begin{cases} \chi_0 = \dfrac{-\chi_1^2 \cdot AR}{\sqrt{AR^2-1}}\kappa \\ \chi_2 = -\dfrac{2}{AR^2-1} - \dfrac{AR}{(AR^2-1)^{3/2}}\kappa \\ \chi_3 = \dfrac{AR^2}{AR^2-1} + \dfrac{AR}{2(AR^2-1)^{3/2}}\kappa \end{cases}$$

with $\kappa = \ln(\frac{AR-\sqrt{AR^2-1}}{AR-\sqrt{AR^2-1}})$. Combined with Eq. (5), the conversion of lift coefficient to the normalized lift force can be expressed as $F_{L,iso} = C_{L,iso} \cdot \frac{Re}{24}$.

Since the Reynolds number and aspect ratio of suspension data to be correlated falls outside the range of Fröhlich et al.'s [1] single particle correlation, we first qualify the extension of the correlation to $Re > 100$ and $AR > 8$. To test the applicability of the correlation at higher Re, comparisons are made with PRS results for an isolated AR2.5 ellipsoid in the flow [19] which shows a peak $C_{L,iso}$ of 0.35 and 0.27 at $Re = 300$ and 1000, respectively. At these conditions Eq. (10-12) yield values of $C_{L,iso} = 0.30$ and 0.24. The relative deviations of 14% and 10.2% implies that though not precise, Eq (10-12) can still provide a reasonable estimation of lift at $Re = 200$. In formulating the dependence of lift on aspect ratio AR, Fröhlich et al. [1] use lift data at $AR = 1.5$, and from $AR = 2$ to 8 in increments of 1, and therefore benefit from dense sampling of the particle geometry. As the geometry of AR10 does not deviate from AR8 dramatically, results of the AR10 ellipsoid can be expected to be reasonably modeled by Eq. (10-12). Note that even though the single particle correlation may exhibit 10% – 15% differences outside its range, the suspension correlation which is developed adjusts for these differences through the fitting parameters.

The proposed suspension correlation builds on Fröhlich et al.'s [1] correlation with the lift coefficient replaced by normalized lift. The proposed correlation is written as:

$$\overline{F}_{L,\theta,cor}(\theta) = 2\overline{F}_{L,\theta,max,cor}\sin(\psi)\cos(\psi) \tag{13}$$

where $\overline{F}_{L,\theta,max,cor}$ is the maximum average lift within inclination angle intervals of $[0°, 10°]$, $[10°, 20°]$ … till $[80°, 90°]$. Two major steps are implemented in the process of proposing the new lift correlation:

1. Modeling the maximum lift for different *Re,* φ and aspect ratio.
2. Replacing the angular dependence $sin(\theta) \cdot cos(\theta)$ by a modified angle $\psi = \{(\frac{\theta}{\frac{\pi}{2}})^{\beta} \cdot \frac{\pi}{2}\}$ with β being a function of *Re,* φ and aspect ratio.

In proposing a new correlation for the maximum lift force, the lift correlation proposed by Sanjeevi & Padding[15] for AR4 sphero-cylinder suspensions is used as reference and can be written as:

$$\overline{F}_{L,\theta,max,cor} = F_{l,iso} \cdot (1-\varphi)^2 + c_1 \cdot \varphi^{0.5} \cdot \left((1-\varphi)^2 + \frac{Re^{1.4}}{(1-\varphi)^2} \right) + \frac{c_2\sqrt{\varphi}}{1-\varphi} + \frac{c_3\varphi}{(1-\varphi)^2} \tag{14}$$

the term $Re^{1.4}$ captures the dependence of maximum lift on the Reynolds number where c_1, c_2 and c_3 are functions of particle aspect ratio:

$$\begin{cases} c_1 = (2.9 + 0.3 \cdot AR) \times 10^{-3} \\ c_2 = 1.0933 \cdot \ln(AR) - 1.534 \\ c_3 = (\ln(10.386 - \frac{14.02}{AR}))^2 \end{cases}$$

The skewness of the lift force data with respect to θ for the ellipsoid suspensions is found to be similar to an isolated particle [1], showing a stronger effect as *Re* and AR increase. On the other hand, an increase in φ tends to rectify skewness of the data and make it more symmetric about $\theta = 45°$. Therefore, a slight modification is made based on the formulation from [1] and β in step 2 takes the form:

$$\beta = \beta_{iso} \cdot (1-\varphi)^{\ln(0.2347 \cdot AR + 2.1375) \cdot \exp(\varphi)} \tag{15}$$

where $\beta_{iso} = (1 + 0.01(ln(AR))^{0.86} \cdot (ln(Re))^{1.77})$ is the skewness rectification for an isolated ellipsoid proposed by Fröhlich et al.[1]. The term $(1-\varphi)^{\ln(0.2347 \cdot AR + 2.1375) \cdot \exp(\varphi)}$ was derived from curve fitting to account for the coupled effect of φ and AR in particle suspensions.

Comparisons of the correlation results with the PRS data with respect to θ for different ellipsoids are presented in Fig. 10. Good agreement can be observed among the different cases as the lift variations are accurately captured by the combination of Eq (13-15) with R-square values for AR2.5, AR5 and AR10 ellipsoids of 0.98, 0.96 and 0.99, respectively. Quantitative analysis of the fitting quality is carried out by calculating the relative deviation for each 10° inclination angle interval using:

$$\varepsilon(\theta) = \frac{|\overline{F}_{L,\theta,cor}(\theta) - \bar{F}_{L,\theta}(\theta)|}{\overline{F}_{L,\theta}(\theta)} \times 100\% \tag{16}$$

As θ approaches 0° or 90°, the $\sin(\psi)\cos(\psi)$ function in Eq (13) leads to diminished $\overline{F}_{L,\theta,cor}$, while in actual suspensions, as is plotted in Fig. 5, scattered lift data with nonzero average exists near these angles. As a consequence, $\varepsilon(\theta)$ at these inclination angles could reach as high as 100% or more, unduly influencing the mean deviation. Hence, the average of $\varepsilon(\theta)$ denoted as $\bar{\varepsilon}(\theta)$ derived from $\varepsilon(\theta)$ over different θ except for those near 0° and 90° is calculated for each suspension. The mean and maximum of $\bar{\varepsilon}(\theta)$ among different *Re* and φ for each aspect ratio are listed in Table 1. A maximum deviation of 13.3% with the mean below 7% indicates the current lift correlation is able to model the lift force for suspensions of ellipsoids with aspect ratio range of [2.5, 10] at $Re \in [10,200]$ and $\varphi \in [0.1,\ 0.3]$. Combined with the isolated ellipsoid correlation of Fröhlich et al. [1], applicability of Eq (13-15) can be extended to $\varphi \in [0, 0.1]$.

Fig. 10. Comparison of lift force with respect to θ between the correlation and PRS results

Table 1. Relative deviation $\bar{\varepsilon}(\theta)$ between the results from PRS simulation and Eq (13-15) of different ellipsoids

Combining the theoretical number density of a random suspension of ellipsoids at different inclination angles given by $sin(\theta)$ with Eq (13), the suspension mean lift can be estimated by:

$$\bar{F}_{L,cor} = \int_{\theta=0}^{90^\circ} 2\sin^2(\theta)\cos(\theta)\overline{F}_{L,\theta,max,cor}d\theta = \frac{2}{3}\overline{F}_{L,\theta,max,cor} \qquad (17)$$

Comparisons of $\bar{F}_{l,cor}$ derived from Eq (17) and $\bar{F}_L$ derived from PRS results are presented in Fig. 11. While $\bar{F}_L$ of AR2.5 ellipsoid is accurately captured by $\bar{F}_{L,cor}$, reasonable agreement also exists for AR5 and AR10 ellipsoid suspensions at $\varphi \leq 0.20$ and $\varphi \leq 0.15$, respectively, beyond which Eq (17) overestimates the suspension mean. The deviation results from the tendency of $\overline{F}_{L,\theta,max}$ shifting towards higher inclination angles as particle aspect ratio or Reynolds number increases. Overall, $\bar{F}_{L,cor}$ calculated from Eq (17) gives a reasonable estimate of the suspension mean lift force $\bar{F}_L$. A more accurate estimation can be done by numerically integrating the full form consisting of Eq (13-15) with the particle number density.

Fig. 11. Comparison of $\overline{F}_L$ obtained from PRS (symbols) with $\bar{F}_{L,cor}$ obtained from Eq (17) (lines) for different ellipsoid suspensions. (Red: AR2.5; Green: AR5; Blue: AR10).

3.3. Correlation for Pitching Torque

Torques $(T_{x'}, T_{y'}, T_{z'})$ about x', y' and z'-directions in the local particle coordinate system are calculated for each ellipsoid in the suspension and presented in Fig. 12 for AR2.5 ellipsoid suspension at $\varphi = 0.3$, $Re = 200$. Smaller dots in the figures represent torque on individual particle while the larger dots with range bars are their angular averages $(\overline{T}_{x',\theta}, \overline{T}_{y',\theta}, \overline{T}_{z',\theta})$ with standard deviations. Similar to the observations made for AR0.25 cylinders [16], the magnitude of $\overline{T}_{x',\theta}$ and $\overline{T}_{y',\theta}$ averaged over 10° intervals are nominally zero at all θ due to the symmetry of the particle geometry with respect to $x' - y'$ plane. Also, the magnitude of $T_{z'}$ is typically larger than $T_{x'}$ and $T_{y'}$ as observed in Fig. 12 for the AR2.5 suspensions. As the long axis of the particle gets larger as with AR5 and AR10 particles, the difference in magnitude is further accentuated. Since the focus of this study is to correlate the mean values, only $T_{z'}$ is considered further.

Fig. 12. Variation of $T_{x'}$, $T_{y'}$ and $T_{z'}$ at different θ in AR2.5 suspensions of $\varphi = 0.3$, $Re = 200$.

To show the effect of aspect ratio, representative results of $T_{z'}$ and $\overline{T}_{z',\theta}$ for AR2.5 and AR10 ellipsoids at $\varphi = 0.2$ and $Re = 200$ are presented in Fig. 13. Large fluctuations, of the same order or much larger than the angular mean are observed especially for AR10 ellipsoids. Compared to the lift forces plotted in Fig. 5, $T_{z'}$ is much more sensitive to the local flow conditions as evidenced from the large fluctuations. This is because torque is dependent on both, the spatial distribution of fluid force on the particle surface which is dictated by the local flow conditions and also on the location of the force or the moment arm from the particle center of mass. As aspect ratio increases, the range of possible moment arm values (both co- and counter-rotating) also increase resulting in larger variations. As a result, Fröhlich et al. [1] have reported that windward tip of AR8 ellipsoid experiences 24 times higher magnitude of toque comparing

435 with surface averaged $T_{z'}$. The general trend in $\overline{T}_{z',\theta}$ is quite similar to $\overline{F}_{L,\theta}$ with a peak value
436 near 45° for AR2.5 but which shifts to higher angles as the aspect ratio increases.

437

438 Fig. 13. Variation of $T_{z'}$ at different θ in AR2.5 and AR10 ellipsoid suspensions.

439 The suspension mean, $\bar{T}_{z'}$, is presented in Fig. 14 (a). $\bar{T}_{z'}$ increases almost linearly with respect to
440 Re with the slope increasing as particle aspect ratio and φ increase. As $T_{z'}$ originates from F_D
441 and F_L multiplied by the moment arm, the near-linear variation of $\bar{T}_{z'}$ could be a result of the
442 super-linear variation of $\bar{F}_L$ (Fig. 7) coupled to the sub-linear variation of $\bar{F}_D$ [27]. $\bar{T}_{z'}$ also
443 increases with both particle aspect ratio and solid fraction of suspension.

444

445 Fig. 14. Suspension mean $\bar{T}_{z'}$ (left) and ratio of the ellipsoid tip acceleration resulting from $T_{z'}$
446 and F_D (right) with respect to Re. (Red: AR2.5; Green: AR5; Blue: AR10.)

447 The significance of fluid torque relative to drag force on particle motion can be approximated by
448 calculating the particle acceleration produced by the rotational torque versus acceleration
449 produced by fluid forces. The ratio of torque induced acceleration to drag induced acceleration is
450 approximated by a phenomenological model which approximates $\alpha^* \approx T^*_{z'}/I^*_{z'z'}$

$$\gamma = \frac{a^*_{T_{z'}}}{a^*_{F_D}} = \frac{\alpha^* \cdot l^*_a}{F^*_D/m^*} = \frac{T^*_{z'}/I^*_{z'z'} \cdot l^*_a}{F^*_D/m^*} = \frac{5l_a}{2(l_a^2 + l_b^2)} \cdot \frac{T_{z'}}{F_D} \tag{18}$$

451 where $a^*_{T_{z'}}$ is the rotational induced acceleration at the tip and $I_{z'z'} = \frac{m^*}{5}(l_a^{*2} + l_b^{*2})$ is the
452 moment of inertia about the local z' - axis of the particle. The ratio γ is derived for each
453 individual particle to obtain the suspension mean ratio $\bar{\gamma}$ which is presented in Fig. 14 (b) with
454 respect to Reynolds number for different particle suspensions. As Re increases, the effect of
455 rotational torque on particle motion becomes more prominent, whereas as φ increases, rotational
456 torque has a lesser effect on particle motion. This is similar to the behavior of lift versus drag
457 forces ($\bar{\xi}$ in Fig. 7). The dependence of $\bar{\gamma}$ on aspect ratio of the particle is more complicated.
458 Both AR2.5 and AR10 suspensions exhibit similar values of $\bar{\gamma}$, both of which are lower than the
459 corresponding $\bar{\gamma}$ at AR5.0. This indicates that as aspect ratio increases above a certain critical
460 limit ($5 \leq AR_{crit} \leq 10$), translational acceleration due to drag force increases faster than the

corresponding torque moment. Overall, $\bar{\gamma} > 0.2$ for $Re \geq 50$, reaching values between 0.38 to 0.85 at $Re = 200$.

To model the variation of $\overline{T}_{z',\theta}$, a functional form similar to the lift correlation is implemented:

$$\overline{T}_{z',\theta,cor}(\theta) = 2\overline{T}_{z',\theta,max,cor}\sin(\psi_T)\cos(\psi_T) \tag{19}$$

where $\psi_T = (\frac{\theta}{\frac{\pi}{2}})^{1.2} \cdot \frac{\pi}{2}$ is a modified angle to capture the location of the peak value for ellipsoids with $AR = 10$. For ellipsoids with $AR \leq 5$, $\psi_T = \theta$. For ellipsoids between $5 < AR \leq 10$, a linear interpolation between 1 and 1.2 is suggested to determine the power of $(\frac{\theta}{\frac{\pi}{2}})$ for a reasonable estimation of the pitching torque skewness. The maximum torque is approximated by modifying the torque on an isolated ellipsoid in flow as follows:

$$\overline{T}_{z',\theta,max,cor} = T_{iso,max}(1-\varphi)^2 + c_4\sqrt{\varphi}\left((1-\varphi)^2 + \frac{Re^{c_5}}{(1-\varphi)^2}\right) + \frac{c_6\varphi}{(1-\varphi)^2} \tag{20}$$

with c_4, c_5 and c_6 being functions of the particle aspect ratios that can be written as:

$$\begin{cases} c_4 = \dfrac{1}{(97.143 \cdot AR - 93.579)^{\frac{1}{2}}} \\ c_5 = 0.1984 \cdot \ln(AR) + 0.7009 \\ c_6 = 1.023 \cdot (AR)^{\frac{1}{2}} - 1.941 \end{cases}$$

$T_{iso,max}$, the maximum torque on an isolated particle is estimated using the correlation from Fröhlich et al. [1]:

$$C_{T,max} = \frac{0.931(\ln(AR))^{0.675}}{Re^{0.162}} + \frac{0.657(\ln(AR))^{2.77}}{Re^{0.178+0.177\ln(AR)}} \tag{21}$$

Here $C_{T,max} = \frac{T^*_{iso,max}}{\frac{1}{2}\rho^* U^{*2}_\infty \frac{\pi d^3_{eq}}{8}}$ is the torque coefficient for an isolated particle in the flow and can be converted to $T_{iso,max}$ using Eq (6). The correlation predictions are compared to the PRS data in Fig. 15. It shows that the PRS results of angular mean torque exhibit a more complex relationship than that implied by Eq (19). In spite of these differences, no attempt has been made to further curve fit the PRS results for the following reasons. Generally, the correlation and PRS agree well for AR2.5 and AR5.0 but deviate from each other at AR10. Difference between PRS and Eq (19) is most visible at low inclination angles ($0° < \theta < 10°$) and at AR10 in the region

$(30° < \theta < 60°)$. At low inclination angles, PRS exhibits higher torque than the correlation, which is due to the small sample size of particles in the interval $(0° < \theta < 10°)$ coupled to the large variation of torque felt by individual particles (see Fig. 12) in the sample. Torques obtained from PRS for AR10 between $(30° < \theta < 60°)$ are not limited by small sample sizes for the angular mean but are prone to large fluctuations in individual particle torques. The leveling off or drop in mean torque at $\theta \approx 45°$ followed by a sharp increase to reach a peak value between 50° and 60° is consistently present across Reynolds numbers and solid fractions and a more complex form of the correlation would be needed to capture this feature at AR10. Considering that the angular mean itself is an approximation to the torque experienced by any individual particle at a particular inclination angle, no attempt is made to change the simple intuitive form of the correlation to capture the angular mean at AR10. Overall, the mean deviation for AR2.5, 5 and 10 ellipsoids over different φ and Re are 8.63%, 28.1% and 36.0%, respectively. A substantial portion of the deviation comes from results at $Re = 10$ due to the low torque magnitude and large observed differences. If $Re = 10$ is not considered then the deviation between PRS and correlation drops to 6.10%, 15.2% and 16.6% for AR2.5, 5 and 10, respectively.

Fig. 15. Comparison of $T_{z'}$ between PRS data averaged within 10° intervals and results derived from Eq (19-21).

Similar to lift, the suspension mean torque can be simply estimated by:

$$\bar{T}_{z',cor}' = \int_{\theta=0}^{90°} 2\sin^2(\theta)\cos(\theta)\overline{T}_{z',\theta,max,cor} d\theta = \frac{2}{3}\overline{T}_{z',\theta,max,cor} \quad (22)$$

from the combination of the sinusoidal fractional distribution of particles with respect to θ and Eq (19). To verity the applicability of Eq (22), the estimated $\bar{T}_{z',cor}'$ at different flow and packing conditions are plotted in Fig. 16 and are compared to the suspension mean torque obtained from the PRS results. Good agreement is found for AR2.5 ellipsoids. As aspect ratio increases to AR5 and AR10, the differences begin to manifest between Eq (22) and PRS results as Re increases mostly because of the uncertainty in modeling the magnitude and location of maximum torque $\overline{T}_{z',\theta,max,cor}$ as is seen in Fig. 15. Overall, Eq (22) can be regarded as a reasonable estimation for $\bar{T}_{z'}'$.

Fig. 16. Comparison between $\overline{T}_z$, obtained from PRS (symbols) with $\overline{T}'_{z',cor}$ obtained from Eq (22) (lines) of different ellipsoid suspensions. (Red: AR2.5; Green: AR5; Blue: AR10)

4. Summary and Conclusions

The paper investigates lift forces and fluid torques acting on prolate ellipsoid suspensions by conducting Particle Resolved Simulations (PRS) in suspensions of aspect ratio (AR) 2.5, 5, and 10, Reynolds number in the range $10 \leq Re \leq 200$ and nominal solid fractions (φ) between $0.1 \leq \varphi \leq 0.3$.

Both, individual particle lift force and pitching torque exhibit large positive and negative variations about the angular mean values. The suspension-mean lift-to-drag force ratio varies between 7% to 14% at Re=10 and increases to 14%~22% at Re=200, demonstrating the non-negligible effect of lift force on particle transport. The relative importance of fluid torque estimated by the ratio of torque induced tip rotational acceleration to the drag force induced translational acceleration, shows that tip rotational acceleration is between 7%~23% of translational acceleration at Re=10 and is consistently larger than 20% at $Re = 50$, reaching 38% ~ 85% at $Re = 200$. The relative importance of both lift force and torque induced rotational acceleration increases as the solid fraction decreases.

To fill a gap in the literature, correlations for modeling mean lift force and torque as a function of particle inclination angle (θ) are developed over the range of AR, Re, and φ investigated in this study. By building both correlations on top of existing correlations for single ellipsoids [1] in flow, the applicability of the correlations is extended to $0 \leq \varphi < 0.3$. The general formulation using $2A\sin(\psi)\cos(\psi)$ is implemented for both lift and torque, A represents the peak value while ψ is a function of θ that adjusts the skewness of the correlation curve to fit PRS data. It is observed that the proposed angular mean lift force correlation captures the PRS data within an average relative percentage deviation below 7% when excluding results near $\theta = 0°$ and $\theta = 90°$ which possess the largest differences due to the near-zero lift forces. As particle aspect ratio increases to AR10, the PRS angular mean torque deviates considerably from the simple canonical form which accentuates the difference with the correlation. Thus, the average deviation in the correlated mean angular torque and PRS data increases to between 8.6% to 36% with the

largest differences manifested at $Re = 10$, the exclusion of which reduces the deviation to between 6.1% to 16.6%.

Acknowledgements

Ze Cao's research was supported in part by an appointment to the U.S. Department of Energy (DOE) Postgraduate Research Program at the National Energy Technology Laboratory administered by Oak Ridge Institute for Science and Education. The authors would like to acknowledge the computational resources provided by Advanced Computational Research (ARC) at Virginia Tech.

References

[1] Fröhlich, K., Meinke, M., and Schröder, W., 2020, "Correlations for Inclined Prolates Based on Highly Resolved Simulations," J. Fluid Mech., **901**, A5.

[2] Ergun, S., 1952, "Fluid Flow through Packed Columns," Chem. Eng. Prog., **48**, pp. 89–94.

[3] Wen, C., and Yu, Y., 1962, "Mechanics of Fluidization," Chem Eng Prog Symp, **62**, pp. 100–111.

[4] Di Felice, R., and Felice, R. D. I., 1994, "The voidage function for fluid-particle interaction systems," Int. J. Multiph. Flow, **20**(I), pp. 153–159.

[5] Tenneti, S., Garg, R., and Subramaniam, S., 2011, "Drag Law for Monodisperse Gas-Solid Systems Using Particle-Resolved Direct Numerical Simulation of Flow Past Fixed Assemblies of Spheres," Int. J. Multiph. Flow, **37**(9), pp. 1072–1092.

[6] Chen, Y., and Müller, C. R., 2018, "Development of a Drag Force Correlation for Assemblies of Cubic Particles : The Effect of Solid Volume Fraction and Reynolds Number," Chem. Eng. Sci., **192**, pp. 1157–1166.

[7] Rong, L. W., Zhou, Z. Y., and Yu, A. B., 2015, "Lattice-Boltzmann Simulation of Fluid Flow through Packed Beds of Uniform Ellipsoids," Powder Technol., **285**, pp. 146–156.

[8] Chen, S., Chen, P., and Fu, J., 2022, "Drag and Lift Forces Acting on Linear and Irregular Agglomerates Formed by Spherical Particles," Phys. Fluids, **34**(2), p.023307.

563 [9] Sommerfeld, M., and Qadir, Z., 2018, “Fluid Dynamic Forces Acting on Irregular Shaped
564 Particles: Simulations by the Lattice–Boltzmann Method,” Int. J. Multiph. Flow, **101**, pp.
565 212–222.

566 [10] Connolly, B. J., Loth, E., and Smith, C. F., 2020, “Shape and Drag of Irregular Angular
567 Particles and Test Dust,” Powder Technol., **363**, pp. 275–285.

568 [11] Sommerfeld, M., and Lain, S., 2018, “Stochastic Modelling for Capturing the Behaviour
569 of Irregular-Shaped Non-Spherical Particles in Confined Turbulent Flows,” Powder
570 Technol., **332**, pp. 253–264.

571 [12] Zastawny, M., Mallouppas, G., Zhao, F., and van Wachem, B., 2012, “Derivation of Drag
572 and Lift Force and Torque Coefficients for Non-Spherical Particles in Flows,” Int. J.
573 Multiph. Flow, **39**, pp. 227–239.

574 [13] Vakil, A., and Green, S. I., 2009, “Drag and Lift Coefficients of Inclined Finite Circular
575 Cylinders at Moderate Reynolds Numbers,” Comput. Fluids, **38**(9), pp. 1771–1781.

576 [14] He, L., and Tafti, D., 2018, “Variation of Drag, Lift and Torque in a Suspension of
577 Ellipsoidal Particles,” Powder Technol., **335**, pp. 409–426.

578 [15] Sanjeevi, S. K. P., and Padding, J. T., 2019, “Hydrodynamic Forces on Assemblies of
579 Non-Spherical Particles: Orientation and Voidage Effects.” AIChE Journal, 66(6),
580 p.16951.

581 [16] Cao, Z., and Tafti, D. K. K., 2020, “Fluid Forces and Torques in Suspensions of Oblate
582 Cylinders with Aspect Ratio 1:4,” Int. J. Multiph. Flow, **131**, p. 103394.

583 [17] Cao, Z. Z., and Tafti, D. K. D. K., 2018, “Investigation of Drag, Lift and Torque for Fluid
584 Flow Past a Low Aspect Ratio (1:4) Cylinder,” Comput. Fluids, **177**, pp. 123–135.

585 [18] Ouchene, R., Khalij, M., Arcen, B., and Tanière, A., 2016, “A New Set of Correlations of
586 Drag, Lift and Torque Coefficients for Non-Spherical Particles and Large Reynolds
587 Numbers,” Powder Technol., **303**, pp. 33–43.

588 [19] Sanjeevi, S. K. P., Kuipers, J. A. M., and Padding, J. T., 2018, “Drag, Lift and Torque
589 Correlations for Non-Spherical Particles from Stokes Limit to High Reynolds Numbers,”

590 Int. J. Multiph. Flow, **106**, pp. 325–337.

591 [20] Clift, R., Grace, J.R., Weber, M. E., 1978, “Bubbles, Drops and Particles,” Chapter 6,
592 Academic Press, New York, 1978.

593 [21] Ouchene, R., Khalij, M., Tanière, A., and Arcen, B., 2015, “Drag, Lift and Torque
594 Coefficients for Ellipsoidal Particles: From Low to Moderate Particle Reynolds Numbers,”
595 Comput. Fluids, **113**, pp. 53–64.

596 [22] Rubinstein, G. J., Ozel, A., Yin, X., Derksen, J. J., and Sundaresan, S., 2017, “Lattice
597 Boltzmann Simulations of Low-Reynolds-Number Flows Past Fluidized Spheres: Effect
598 of Inhomogeneities on the Drag Force,” J. Fluid Mech., **833**, pp. 599–630.

599 [23] Rubinstein, G. J., Derksen, J. J., and Sundaresan, S., 2016, “Lattice Boltzmann
600 Simulations of Low-Reynolds-Number Flow Past Fluidized Spheres: Effect of Stokes
601 Number on Drag Force,” J. Fluid Mech., **788**, pp. 576–601.

602 [24] Tafti, D.K., 2001, November. "GenIDLEST: A scalable parallel computational tool for
603 simulating complex turbulent flows," In ASME International Mechanical Engineering
604 Congress and Exposition (Vol. 35722, pp. 347-356). American Society of Mechanical
605 Engineers.

606 [25] Tafti, D. K., 2011, “Time-Accurate Techniques for Turbulent Heat Transfer Analysis in
607 Complex Geometries." Computational fluid dynamics and heat transfer, pp. 217–264.

608 [26] Cao, Z., and Tafti, D. K., 2021, “Convective Heat Transfer in Suspensions of Prolate
609 Ellipsoids,” Int. J. Heat Mass Transf., **177**, p. 121575.

610 [27] Cao, Z., Tafti, D. K., and Shahnam, M., 2020, “Development of Drag Correlation for
611 Suspensions of Ellipsoidal Particles,” Powder Technol., **369**, pp. 298–310.

612 [28] Cao, Z., Tafti, D. K., and Shahnam, M., 2021, “Modeling Drag Force in Ellipsoidal
613 Particle Suspensions with Preferential Orientation,” Powder Technol., **378**, pp. 274–287.

614 [29] Nagendra, K., Tafti, D. K., and Viswanath, K., 2014, “A New Approach for Conjugate
615 Heat Transfer Problems Using Immersed Boundary Method for Curvilinear Grid Based
616 Solvers,” J. Comput. Phys., **267**, pp. 225–246.

[30] Nvidia, “NVIDIA PhysX SDK 3.3.4 Documentation.”

[31] He, L., Tafti, D. K., and Nagendra, K., 2017, “Evaluation of Drag Correlations Using Particle Resolved Simulations of Spheres and Ellipsoids in Assembly,” Powder Technol., **313**, pp. 332–343.

[32] Brown, P. P., and Lawler, D. F., 2003, “‘Free-Flight Measurements of Sphere Drag and Settling Velocity Revisited,” J. Environ. Eng., **129**(3), pp. 222–231.

[33] Wittig, K., Richter, A., and Golia, A., 2014, “CD and Nu Closure Relations for Spherical and Nonspherical Particles,” Gasif. Process. Model. Simul., pp. 73–104.

[34] Rosemann, T., Reinecke, S. R., and Kruggel-Emden, H., 2021, “Analysis of Mobility Effects in Particle-Gas Flows by Particle-Resolved LBM-DEM Simulations,” Chemie-Ingenieur-Technik, **93**(1–2), pp. 223–236.

[35] Happel, J., and Brenner, H., 1983, “Low Reynolds Number Hydrodynamics,” Englewood Cliffs NJ, **40**(1), pp. 25–45.

[36] Hölzer, A., and Sommerfeld, M., 2009, “Lattice Boltzmann Simulations to Determine Drag, Lift and Torque Acting on Non-Spherical Particles,” Comput. Fluids, **38**(3), pp. 572–589.

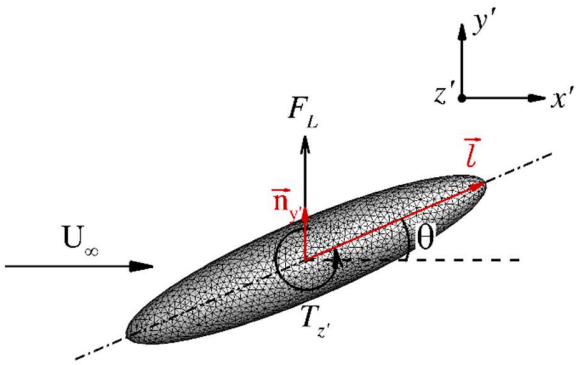

Fig. 1. Local Cartesian coordinate system with the definition of lift and torque for AR5 ellipsoid

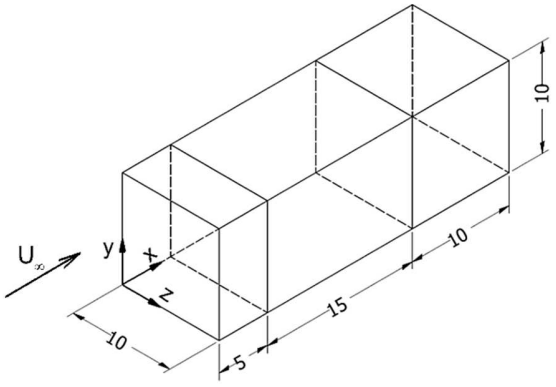

Fig. 2. Computational domain for the PRS simulations.

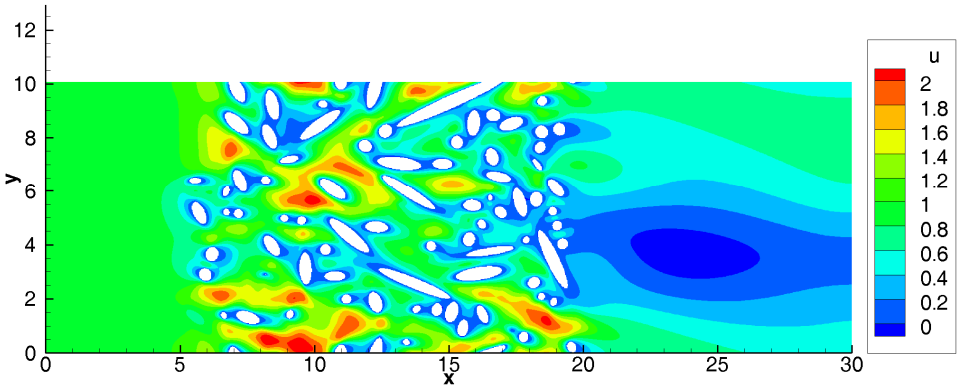

(a) u velocity distribution at $Re = 10$

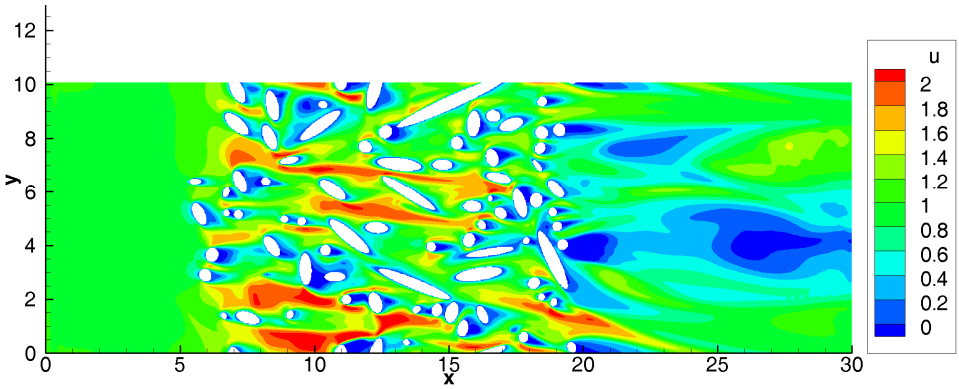

(b) u velocity distribution at $Re = 200$

Fig. 3. u-velocity distribution in AR10 ellipsoid suspension at φ=0.1

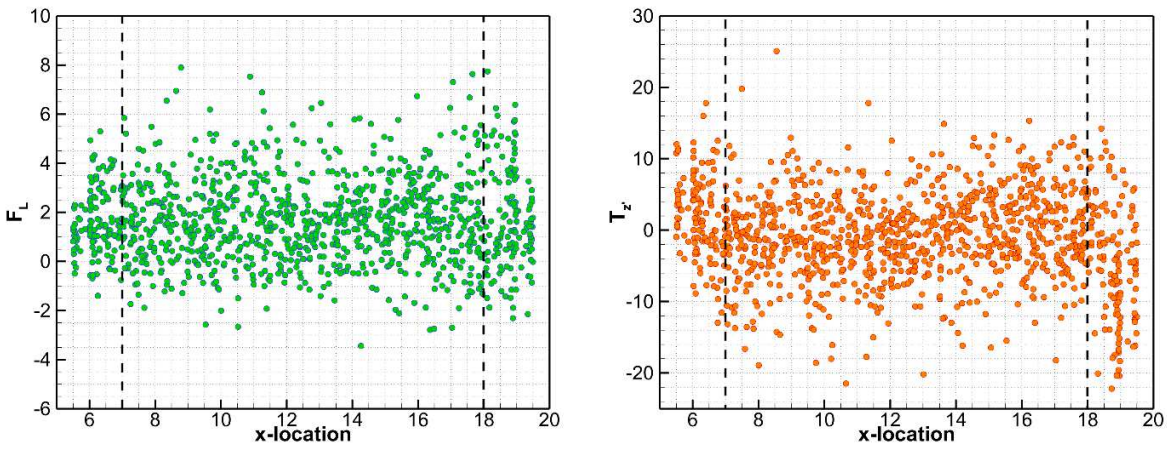

(a) Particle lift force, F_L (b) Particle torque, $T_{z'}$

Fig. 4. Individual AR10 ellipsoid F_L and $T_{z'}$ with respect to their centroid x-location in suspension with $\varphi = 0.2$, $Re = 10$

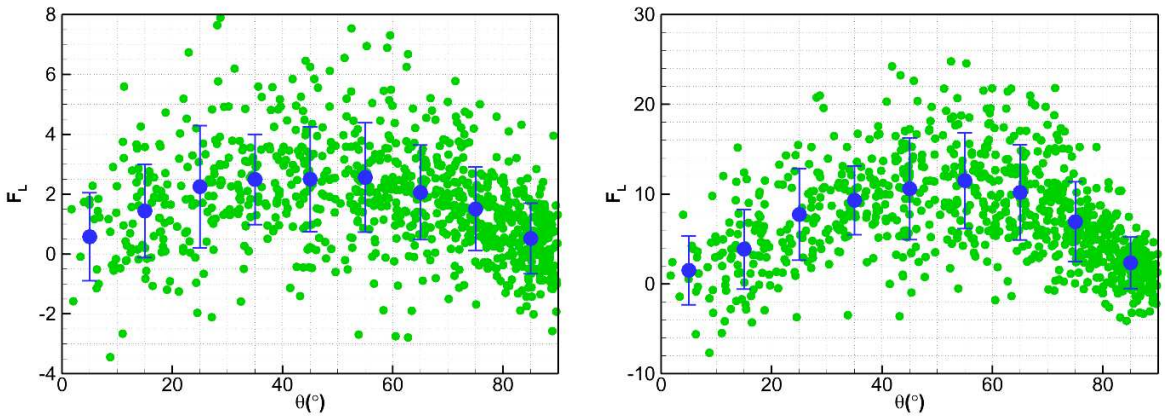

(a) Lift at $Re = 10$ (b) Lift at $Re = 200$

Fig. 5. Individual (F_L) and inclination mean lift forces ($\bar{F}_{L,\theta}$) with standard deviation of AR10 ellipsoid suspension at $\varphi = 0.2$

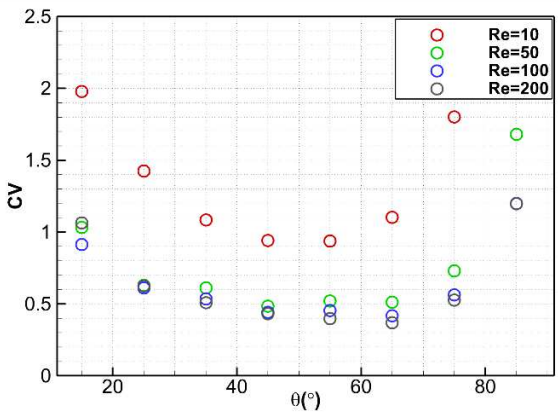

(a) AR2.5 ellipsoid, $\varphi = 0.1$

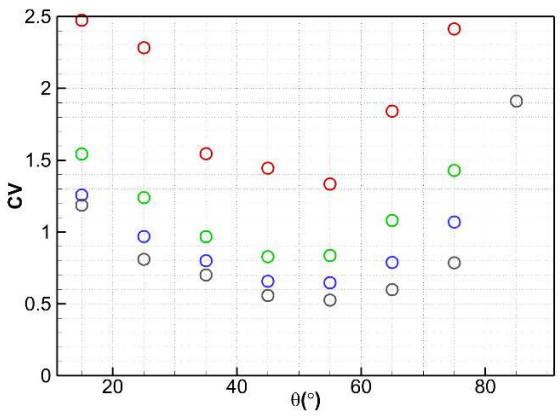

(b) AR2.5 ellipsoid, $\varphi = 0.3$

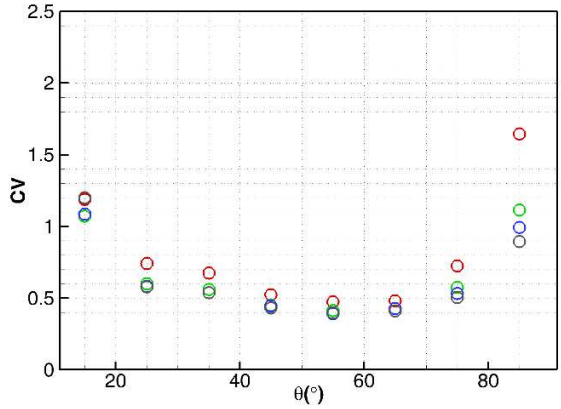

(c) AR10 ellipsoid, $\varphi = 0.1$

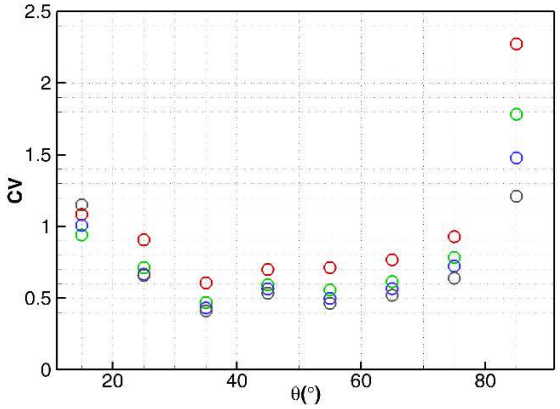

(d) AR10 ellipsoid, $\varphi = 0.2$

Fig. 6. Coefficients of variation (CV) with respect to θ for different particle suspensions

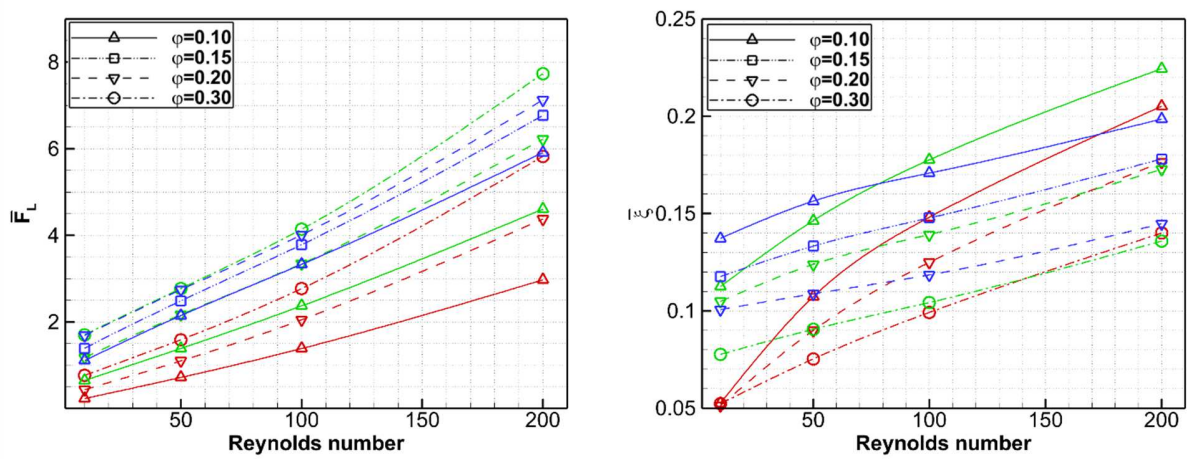

(a) $\bar{F}_L$ of different ellipsoid suspensions (b) $\bar{\xi}$ of different ellipsoid suspensions

Fig. 7. Suspension mean lift force of different ellipsoids. (Red: AR2.5 ellipsoid; Green: AR5 ellipsoid; Blue: AR10 ellipsoid)

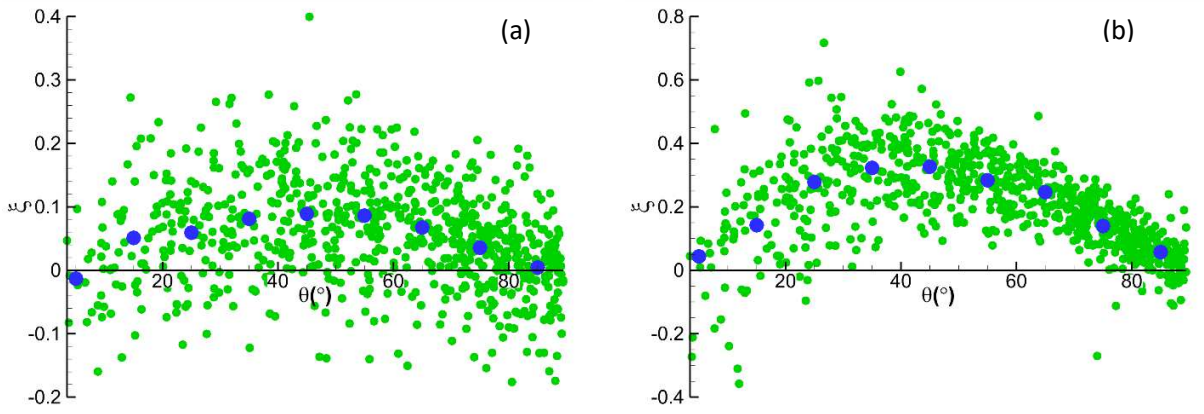

Fig. 8. Individual and averaged particle lift/drag ratio in AR2.5 ellipsoid suspension at $\varphi = 0.1$, $Re = 10$ (left) and 200(right).

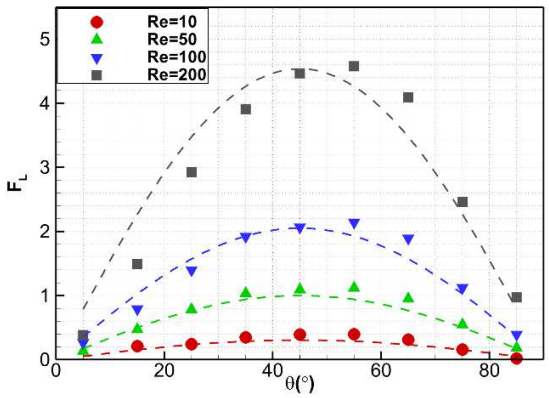

(a) AR2.5, φ = 0.1

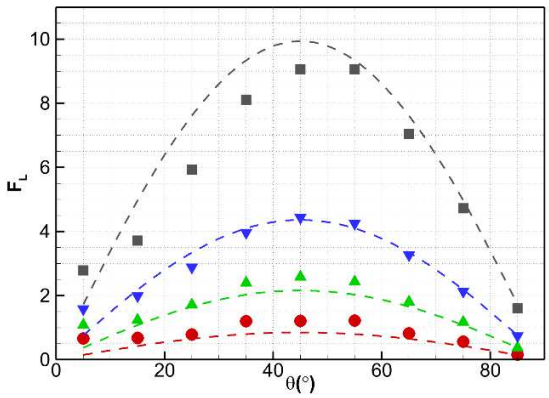

(b) AR2.5, φ = 0.3

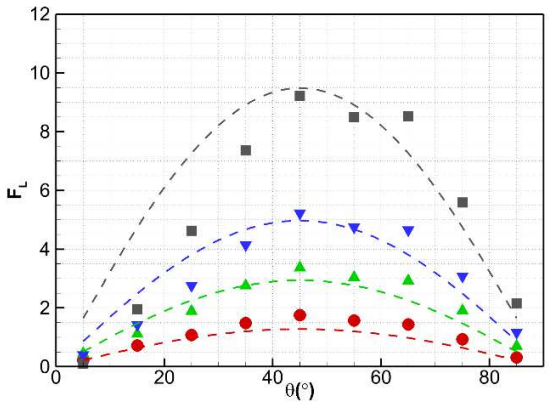

(c) AR10, φ = 0.1

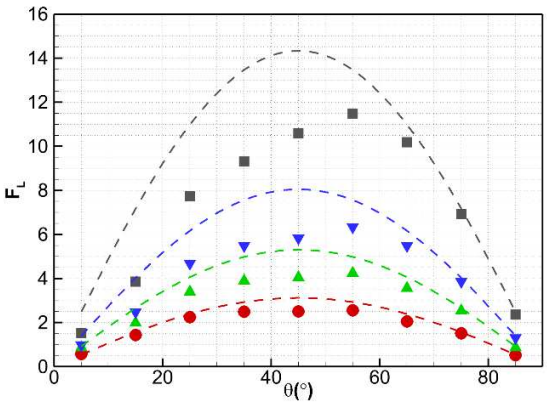

(d) AR10, φ = 0.2

Fig. 9. Comparison of F_L derived from PRS simulation and Eq (8) for different ellipsoid suspensions

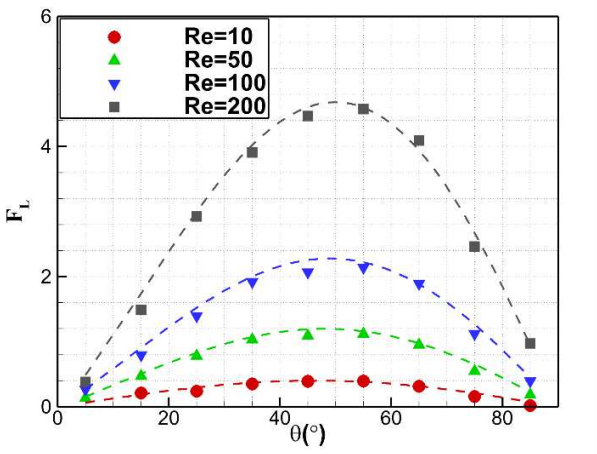

(a) AR2.5, φ = 0.1

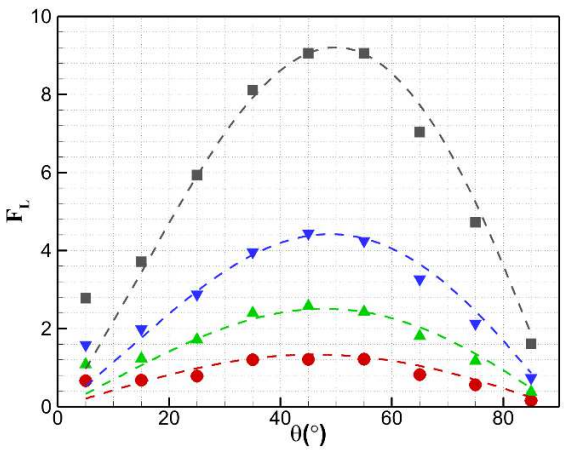

(b) AR2.5, φ = 0.3

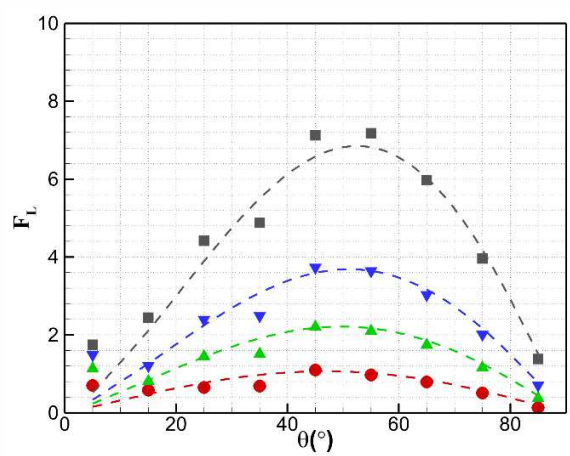

(c) AR5, φ = 0.1

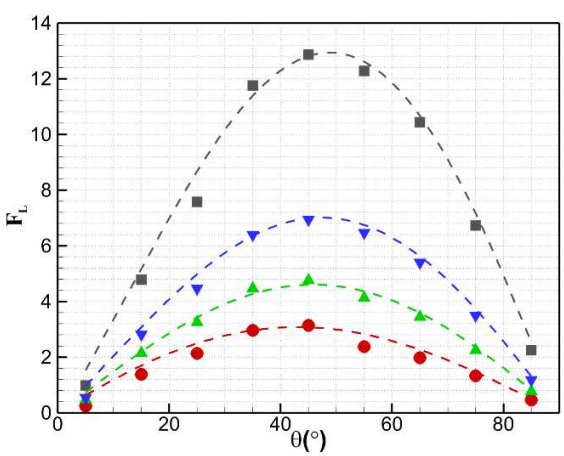

(d) AR5, φ = 0.3

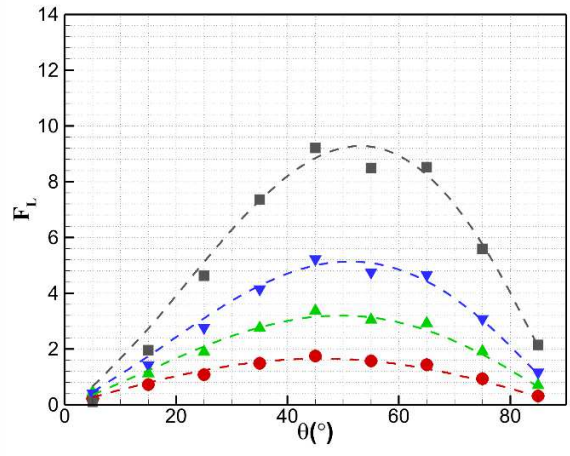

(e) AR10, φ = 0.1

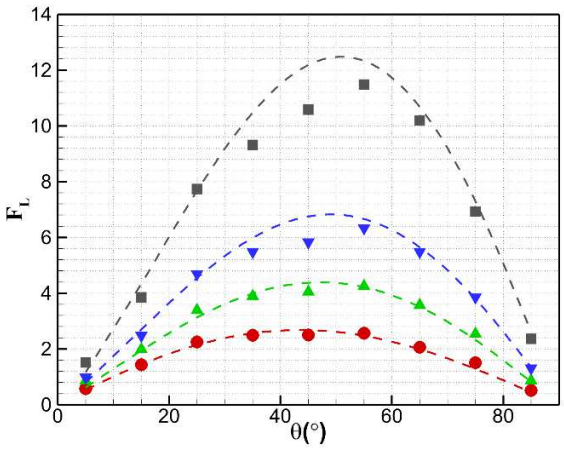

(f) AR10, φ = 0.2

Fig. 10. Comparison of lift force with respect to θ between the correlation and PRS results

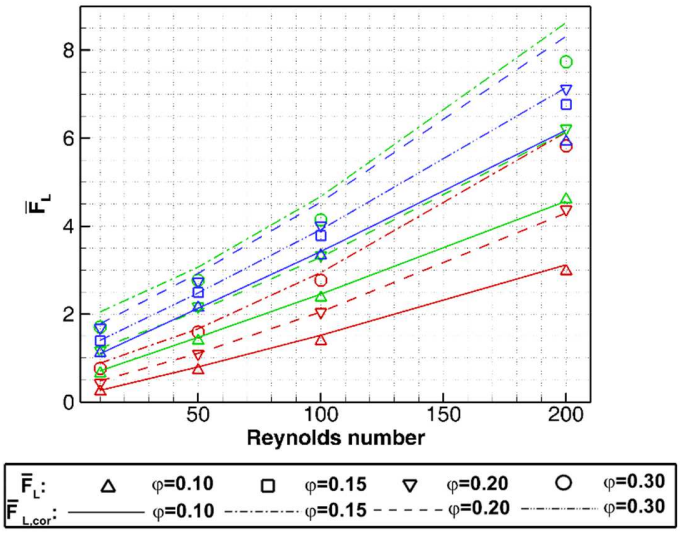

Fig. 11. Comparison of $\overline{F}_L$ obtained from PRS (symbols) with $\overline{F}_{L,cor}$ obtained from Eq (17) (lines) for different ellipsoid suspensions. (Red: AR2.5; Green: AR5; Blue: AR10).

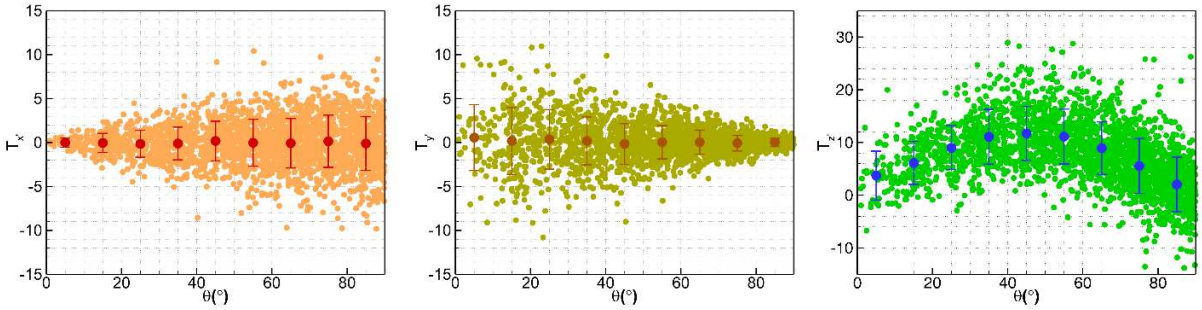

(a) Results of T_x' (b) Results of T_y' (c) Results of T_z'

Fig. 12. Variation of $T_{x\prime}$, $T_{y\prime}$ and $T_{z\prime}$ at different θ in AR2.5 suspensions of $\varphi = 0.3$, $Re = 200$.

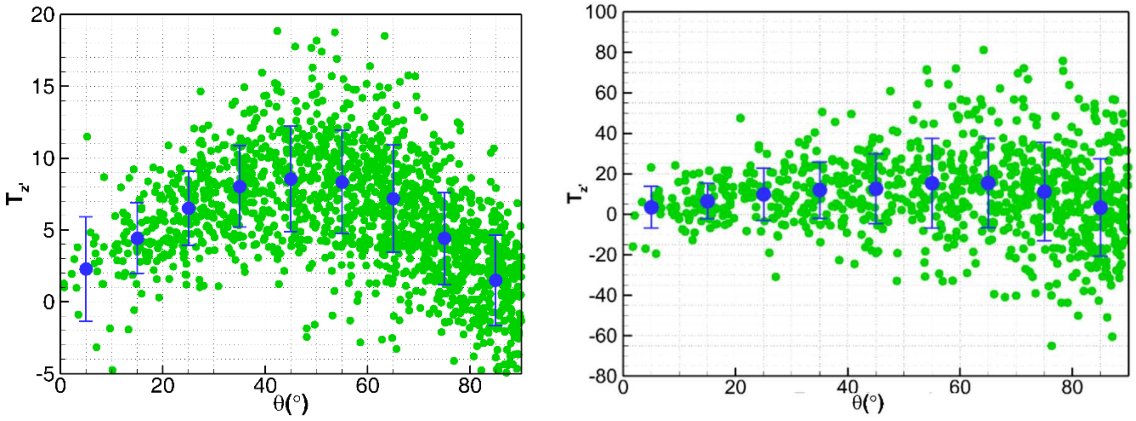

(a) AR2.5 ellipsoid at $Re = 200$, $\varphi = 0.2$ (b) AR10 ellipsoid at $Re = 200$, $\varphi = 0.2$

Fig. 13. Variation of $T_{z'}$ at different θ in AR2.5 and AR10 ellipsoid suspensions.

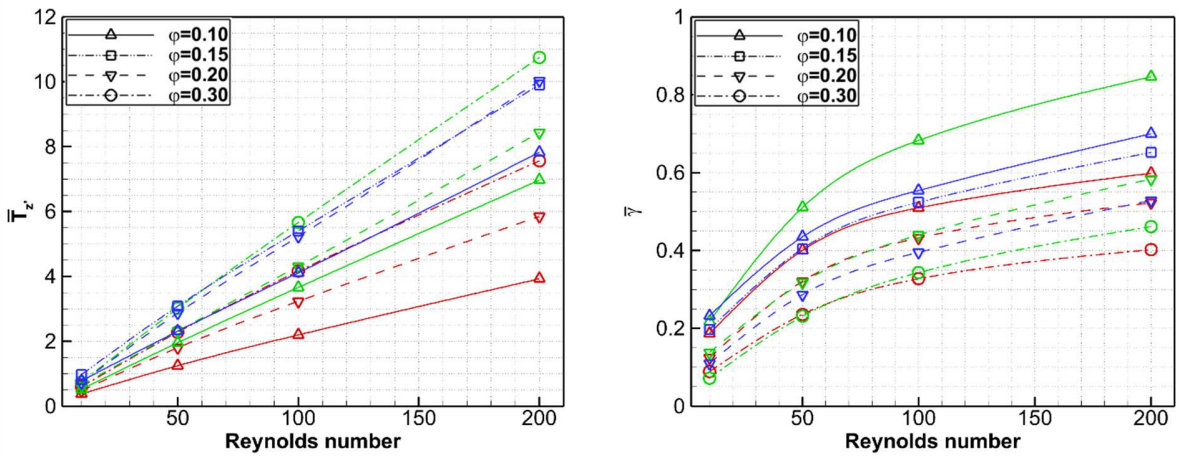

(a) $\overline{T}_{z'}$ of different ellipsoid suspensions

(b) $\bar{\gamma}$ of different ellipsoid suspensions

Fig. 14. Suspension mean $\overline{T}_{z'}$ (left) and ratio of the ellipsoid tip acceleration resulting from $T_{z'}$ and F_D (right) with respect to Re. (Red: AR2.5; Green: AR5; Blue: AR10.)

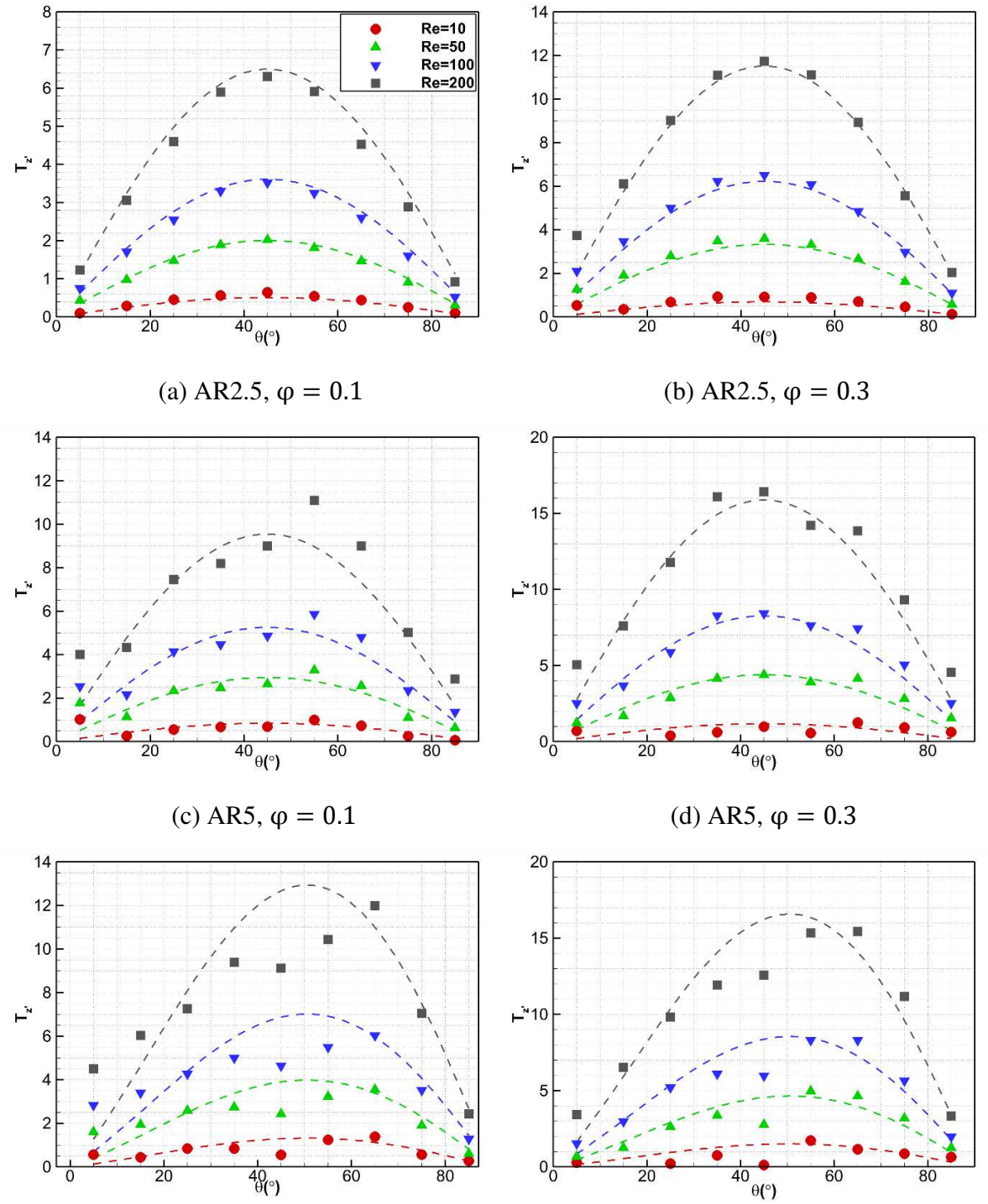

(a) AR2.5, φ = 0.1

(b) AR2.5, φ = 0.3

(c) AR5, φ = 0.1

(d) AR5, φ = 0.3

(e) AR10, φ = 0.1

(f) AR10, φ = 0.2

Fig. 15. Comparison of $T_{z'}$ between PRS data averaged within 10° intervals and results derived from Eq (21-23).

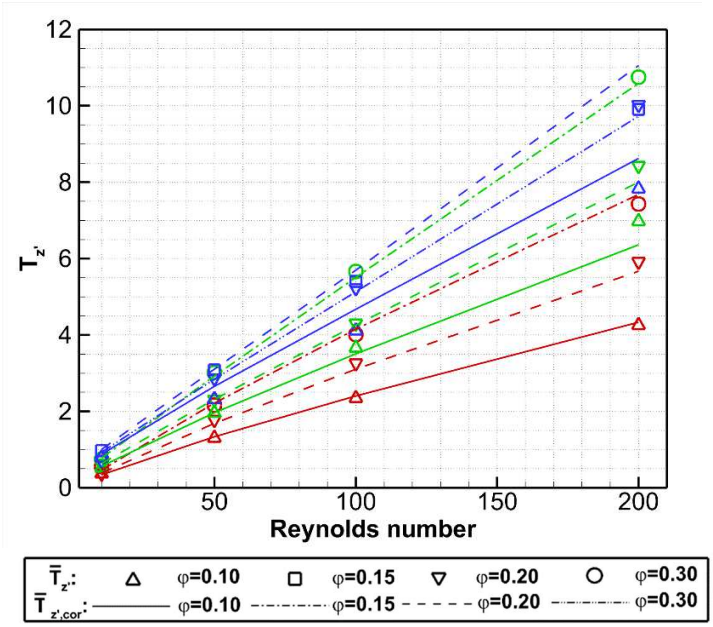

Fig. 16. Comparison between $\overline{T}_{z'}$ obtained from PRS (symbols) with $\bar{T}'_{z',cor}$ obtained from Eq (22) (lines) of different ellipsoid suspensions. (Red: AR2.5; Green: AR5; Blue: AR10)

Table 1. Relative deviation $\bar{\varepsilon}(\theta)$ between the results from PRS simulation and Eq (13-15) of different ellipsoids

	Mean $\bar{\varepsilon}(\theta)$	Maximum $\bar{\varepsilon}(\theta)$
AR2.5	6.83%	13.3%
AR5	7.02%	12.1%
AR10	6.51%	9.0%

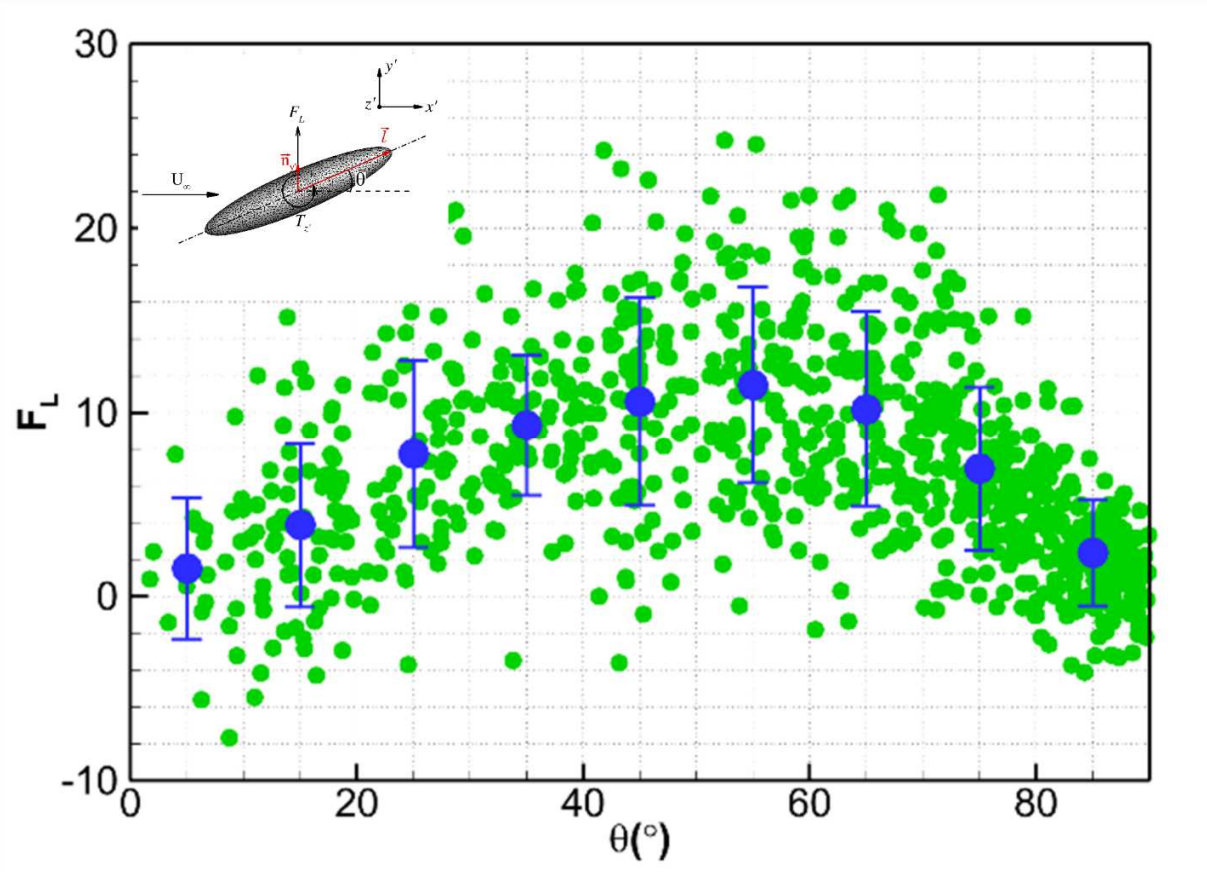
30
20
10
0
-10
0
20
40
60
80
θ(°)
F_L
U∞
y'
z'
x'
F_L
n
l
θ
T_z'